

The Near Infrared Sky Background

N. Pirzkal
May 13, 2014

ABSTRACT

WFC3 IR observations are often background limited. In the vast majority of cases, when HST is pointed away from the Earth Limb, the main contribution to this background light is caused by zodiacal infrared light, including the Gegenschein, the diffuse glow in the sky centered upon Earth's antisolar point. In this ISR, we present direct measurements of the infrared background levels as observed by WFC3 since its launch and in several broad band filters. We compare our observations to the values currently used in the Exposure Time Calculator (ETC) and derive a model of the IR background levels as a function of Ecliptic Latitude and Sun Angle.

Data and Analysis

WFC3 IR images have been continuously monitored since the installation of WFC3 on board of HST, as part of the “Blob” Monitoring Program (Pirzkal et al. 2012) and the making of deep sky-flats (Pirzkal et al. 2011). The data that were used and details of the procedures used are given in Pirzkal et al. 2011 and Pirzkal et al. 2012. As part of this routine monitoring, we naturally needed to accurately measure the background level in each of the available infrared exposures. This was done by first generating an object mask using SExtractor for each individual FLT file. This mask was then used to mask out sources in each of the IMSET of the original IMA file and we then computed the background in each IMSET

of the IMA files, ignoring pixels with known objects. Using the IMA files instead of the FLT files allowed us to better time sample the observed background of HST as it was potentially pointing close to the Earth limb, i.e. allow us to detect sudden rise or decrease in background levels during the course of an exposure. We estimated that a minimum exposure time of 100 seconds, and a minimum of 10^5 pixels was sufficient to determine the background level of an individual exposure. Our 100 second minimum integration time requirement corresponds to more than $50 e^-$ per pixel and hence a signal-to-noise per pixel > 7 . Besides ignoring pixels affected by celestial sources, as and we did when looking for “Blobs”, both known bad pixels (using the DQ array content) as well as pixels affected by persistence (See Long et al. 2010) were also masked out. More details about how pixels affected by persistence were flagged is available in Pirzkal et al. 2011. Finally, we found that images affected by very large scale structure (such as diffuse astronomical sources and light from the Earth limb) could be identified and discarded by requiring the mean and mode values computed for an exposure to be within 1% of each other. Finally, we also avoided using the large number of images taken within 5 degrees of the Orion Nebula (M42) which is at coordinates of 05:35:17.3 and -05:23:28. The later is a very extended source that was extensively observed using WFC3 and which resulted in images containing very high levels of nebular emission and that are not suitable for our study. We estimated the background level of several thousands individual exposures and the exact numbers for individual filters are listed in Table 1. In addition to computing the mean background of each exposure we also kept track of the accurate Sun Angle and other related HST pointing information using the associated jitter information (JIT file). Each JIT file contains a time series of the orientation and pointing of HST during the course of an exposure. Using the RA and DEC values of the V1 axis of HST (i.e. where HST was pointing), we were able to compute the ecliptic latitude and longitude at the center of each of these images. The Python module *pyephem* was used to convert RA and DEC coordinates of the field into ecliptic coordinates. The data were then grouped by filters, as shown in Table 1, and the minimum background level at a given ecliptic position was assumed to be a good representation of the underlying true zodiacal light level. To increase the signal to noise of our measurements we binned them in Sun Angle and ecliptic Latitude bins of 10 degrees. We show the F125W and F160W backgrounds in Figure 1.

Filter Dependence

We found that the shape of the zodiacal background rate as a function of Sun angle and ecliptic Latitude was mostly uncorrelated with wavelength. The same distributions were observed using all of the filters we listed in Table 1. Once scaled to account for bandpass differences, we measured less than 20% variation on the background levels measured using

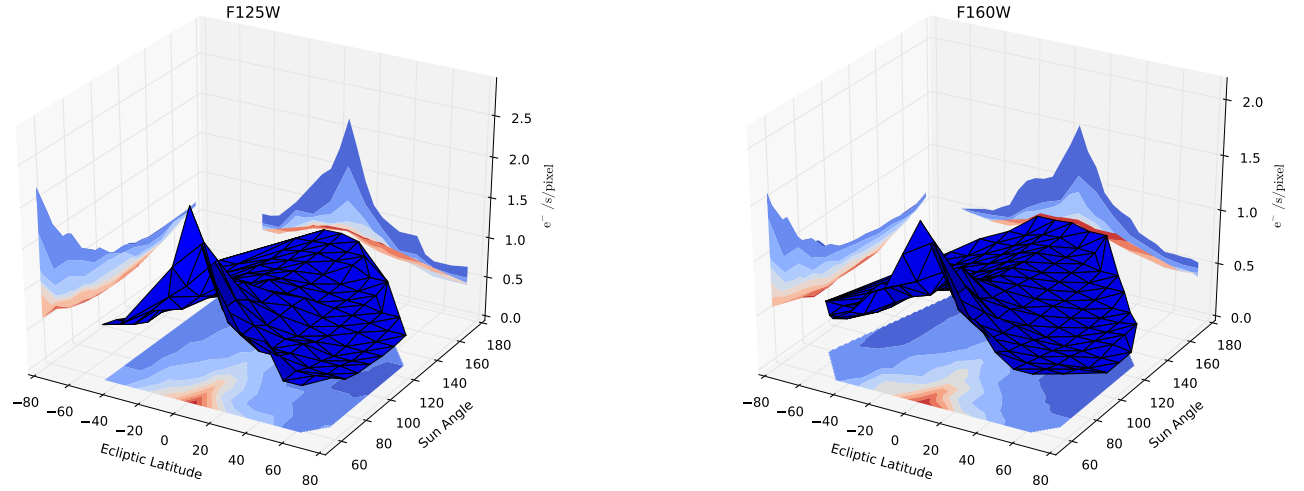


Fig. 1.— The measured F125W (left) and F160W (right) IR backgrounds in $e^-/s/pixel$, plotted as a function of ecliptic latitude and Sun angle. The zodiacal light background increases rapidly at small Sun angle values. The shapes of the observed background levels, as seen using different broad band filters, differ only by a scaling constants (Listed in Table 1).

Filter	Number of FLTs	Number of IMSETs	Scaling Factor
<i>F098M</i>	485	1160	0.66 ± 0.10
<i>F105W</i>	773	1562	1.21 ± 0.20
<i>F110W</i>	744	1480	1.97 ± 0.37
<i>F125W</i>	1319	2004	1.13 ± 0.11
<i>F140W</i>	410	579	1.50 ± 0.14
<i>F160W</i>	3038	4673	1.00
<i>G141</i>	1160	3535	2.06 ± 0.27

Table 1: *Number of individual FLT files included in this ISR for each of the filter we considered. We also list the number of IMSETs (readout) in the associated IMA files that we used to measure background levels. We only measured the background level of individual extensions (i.e. readouts) of IMA files with a cumulative sample time greater than 100 seconds. The last column of this Table lists the average background levels, in $e^-/s/pixel$, normalized to our observations in the F160W background.*

different filters. We conclude that as a good approximations, all of the observations can be scaled appropriately to match those taken in filter F160W. For the remainder of this ISR, we therefore restrict ourselves to the background rate distribution for the F160W filter. All other zodiacal background rates can be computed by multiplying our estimates by the scaling factors shown in Table 1. As we show in Table 1, the F098M filter background is 0.66 times that of the F160W filter, while the background level as seen by the F110W filter is 1.97 times higher than when using the F160W filter. Note that the background levels are in $e^-/s/pixel$. Table 1 also lists the background level for the G141 slitless grism. While we did not include data from the G141 in our analysis, we found that the distribution of the G141 zodiacal background is also very similar to what is observed using the broad band filters. To a first approximation, and for observations not affected by the bright Earth limb (i.e. if we exclude abnormally high background observations), the background level in the G141 is about ≈ 2.06 than in the F160W filter. Since all of our measurements were consistent, we opted to combine all measurements together using the scale factors listed in Table 1. We therefore computed an average value and its standard deviation for the observed F160W background at each sun angle and ecliptic latitude, using a 2σ rejection criterion to remove dubious measurements. Figure 2 shows both the observed average background (left panel, scaled to the F160W filter) as well as the associated errors (right panel). As this Figure shows, the uncertainties are typically on the order of 10% or better.

Comparison with Exposure Time Calculator

We compared our measured background values to those generated by the ETC (Version 22.1.2) . The ETC values were taken from Table 2 at <http://etc.stsci.edu/etc/help/background> and from Giavalisco et al. 2002. We converted the listed V AB magnitudes to approximate count rates in the F160W filter using the ETC itself. All of our background measurements were normalized by the values listed in Table 1 so that we could combine all of them together in order to increase the number of available samples. Any remaining discrepancies between the ETC background count rates and our observations are thus a reflection of significant differences in the general shape of the function describing the zodiacal background as a function of position (Sun Angle and Heliocentric Latitude in this case). As we show in the top two panels of Figure 3. Panel (a) shows the difference between the ETC count rates and our observations and shows a difference greater than $1e^-/s$ when pointing close to the Sun (Low Sun Angle value and a latitude close to zero). Fractionally, and as shown in Panel (b), this is a discrepancy close to 100%. Below panels (a) and (b) we show histograms of the fitting residuals that are displayed in panels (a) and (b). Overall, the ETC values appear to be most discrepant with our observations in the Sun and anti-Sun directions, with as much as 100% disagreements.

Fitting

The Solar Mass Ejection Imager (SMEI) has observed both the zodiacal and Gegenschein, the diffuse glow in the sky centered upon Earth’s antisolar point, in the optical wavelength and down to a precision of $\approx 1\%$. In Buffington et al. 2009, the authors analytically fitted their observations, which are based on several thousands measurements and an angular resolution of 0.5 degree over a period of 5 years. The Buffington et al. observations are a good match to what we see with WFC3 in the infrared and we thus fitted the light distribution shown in Figure 1 to a slightly modified version of the functional form introduced by Buffington et al. We thus fitted the data described in Section and shown in Figure 2 to the function

$$Z(\lambda, \beta) = a_0 + a_{10}(Z_1(\lambda, \beta) + Z_2(\lambda, \beta) + G(\lambda, \beta)) \quad (1)$$

where

$$Z_1(\lambda, \beta) = a_0 + a_1(1 - \cos b(\beta)) + (a_2 + a_3c(\lambda, \beta) + a_4c(\lambda, \beta)^2 + a_5c(\lambda, \beta)^3) \times 10^{-\frac{\sin(B(\beta))}{a_6(e(\lambda, \beta) + a_7)}} \quad (2)$$

$$Z_2(\lambda, \beta) = a_7e^{\frac{-\beta^2}{a_8}} \quad (3)$$

and

$$c(\lambda, \beta) = \cos(\lambda) \times \cos(\beta) \quad (4)$$

$$B(\beta) = 1.5 \times (\sqrt{(1 + (\beta/1.5)^2} - 1) \quad (5)$$

$$e(\lambda, \beta) = \arccos(c(\lambda, \beta)) \quad (6)$$

and where $G(\lambda, \beta)$ is the Gegenschein enhancement term taken directly from equation 7 in Buffington et al. 2009.

Results

The fitting process was started by first setting the variables a_1 through a_9 to the values listed in Buffington et al. and simply shifting and scaling the SMEI background model using the variables a_0 and a_{10} , as is shown in Equation 1. Once optimal values for a_0 and a_{10} were found ($a_0 = 0.2420$ and $a_{10} = 0.0055$), and a reasonable match of the SMEI model to our data was found, we further fitted Equation 1 to our observations and allowed for all 11 parameters to be fitted. A Markov Chain Monte Carlo approach was used for this final step. Our final estimates for the values of a_i are shown in Table 2. The global RMS of the fit is 10.5% and the fit is a good representation of the observations.

a_i	value
a_0	0.2244
a_1	0.3147
a_2	0.4250
a_3	0.5183
a_4	0.8650
a_5	0.5743
a_6	0.0142
a_7	53.793
a_8	0.0248
a_9	608.635
a_{10}	0.0051

Table 2: *Values of the a_i parameters in Equation 1*

The values listed in Table 2 and Equation 1 allow one to predict the expected zodiacal IR background in the F160W filter. Background levels in other filters can be determined by

scaling the F160W results by the scaling factors listed in Table 1. Figure 4 show the average F160W levels as a function of Sun Angle and Ecliptic Latitude.

Comparison our Fit to the observations

In the bottom two panels of Figure 3, we performed the same comparison between models and observations that was discussed in Section . The results obtained using Equation 1 and the values listed in Table 2 are shown in the bottom two panels (c and d). We plotted these directly below Panels (a) and (b) so that they could all be compared directly. As the bottom two panels show, the residuals between observations and our model are less than half of what they are when comparing them to the current ETC values. While there are still some discrepancies when pointing close to the Sun, these are now much smaller. The overall fit is also improve in the anti-Sun direction, as well as globally.

Conclusion

We measured the observed background levels in several thousands of archival WFC3 observations. Using these measurements, we determined that the shape of the near-infrared background, as a function of heliocentric latitude and Sun Angle, was mostly wavelength independent and differed only by a scaling factor. Comparing these new observations to the data used by the ETC show discrepancies by as much as 100%. In absolute terms, these discrepancies remain however small and on the order of less than $1e^-/s/pixel$. We fitted our observations to an analytical function that describes the contributions of both the zodiacal light and of the Gegenschein and derived a good fit to the WFC3 observations. Overall, our new description of the zodiacal background levels are within 10% of our observations and a significant improvement over the current ETC.

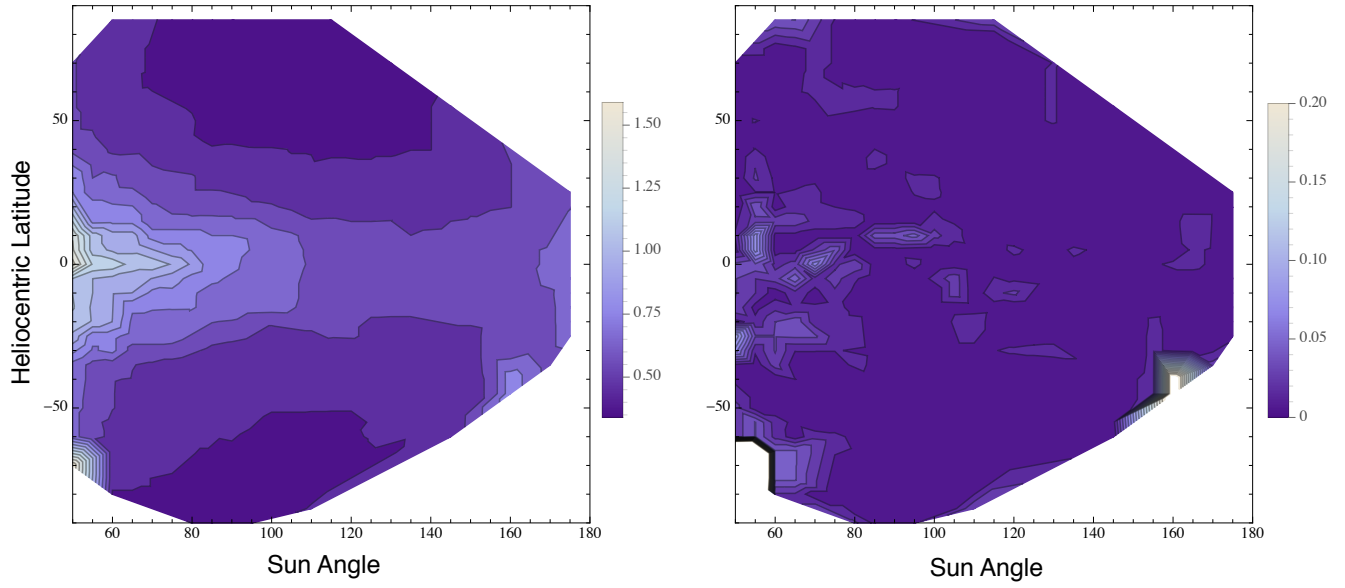


Fig. 2.— The average F160W filter background levels (left panel) and their fractional uncertainties (right panel). These were computed by combining all available data, after accounting for the scale factors listed in Table 1.

References

- Buffington A. et al., 2009, ICARUS, 203, 124
- Giavalisco M., Kailash S., Bohlin R. C. 2002, WFC3 ISR 2002-12
- Long K. S., Baggett S., Deustua S., Reiss A. *WFC3/IR Persistence as Measured in Cycle 17 using Tungsten Lamp Exposures*, WFC3 ISR 2010-17
- Pirzkal N., Viana A., Rajan A. *The WFC3 “Blobs”*, WFC3 ISR 2010-06
- Pirzkal N., Mack J., Dahlen T., Sabbi E. *Sky Flats: Generating Improved WFC3 IR Flat-fields*, WFC3 ISR 2011-11
- Pirzkal N., Hilber B. *The WFC3 IR “Blobs” Monitoring*, WFC3 ISR 2012-15

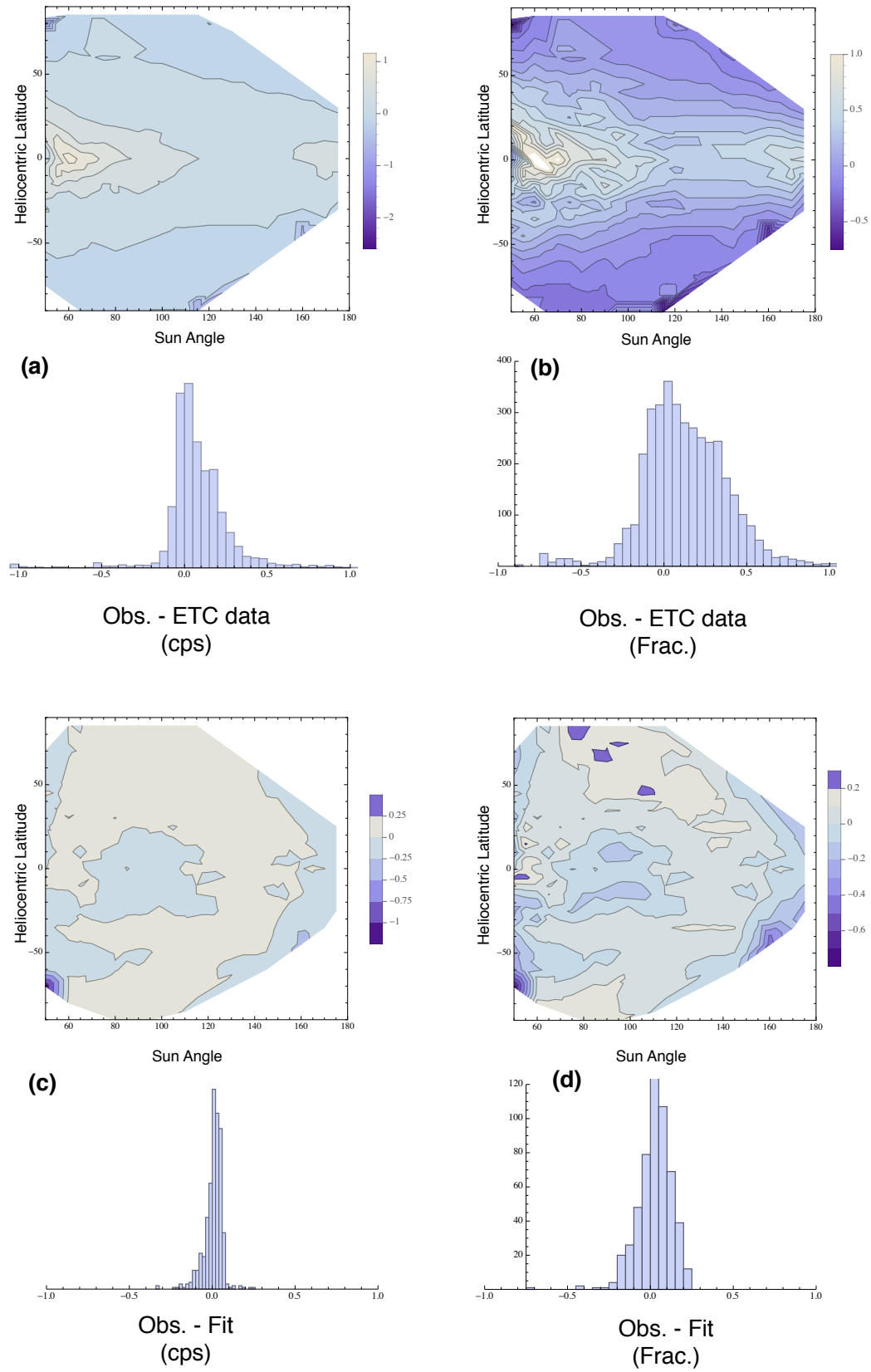


Fig. 3.— Panels a and b: The background we measured compared to the current ETC estimates, in $e^-/s/pixel$ (left) and fractional (right). Histograms are shown at the bottom of each panel. Panels c and d: Same as the panels above but now comparing the background levels we measured to the functional fit from Equation 1 with the values shown in Table 2. A significant improvement is obtained, especially at small Sun Angle values.

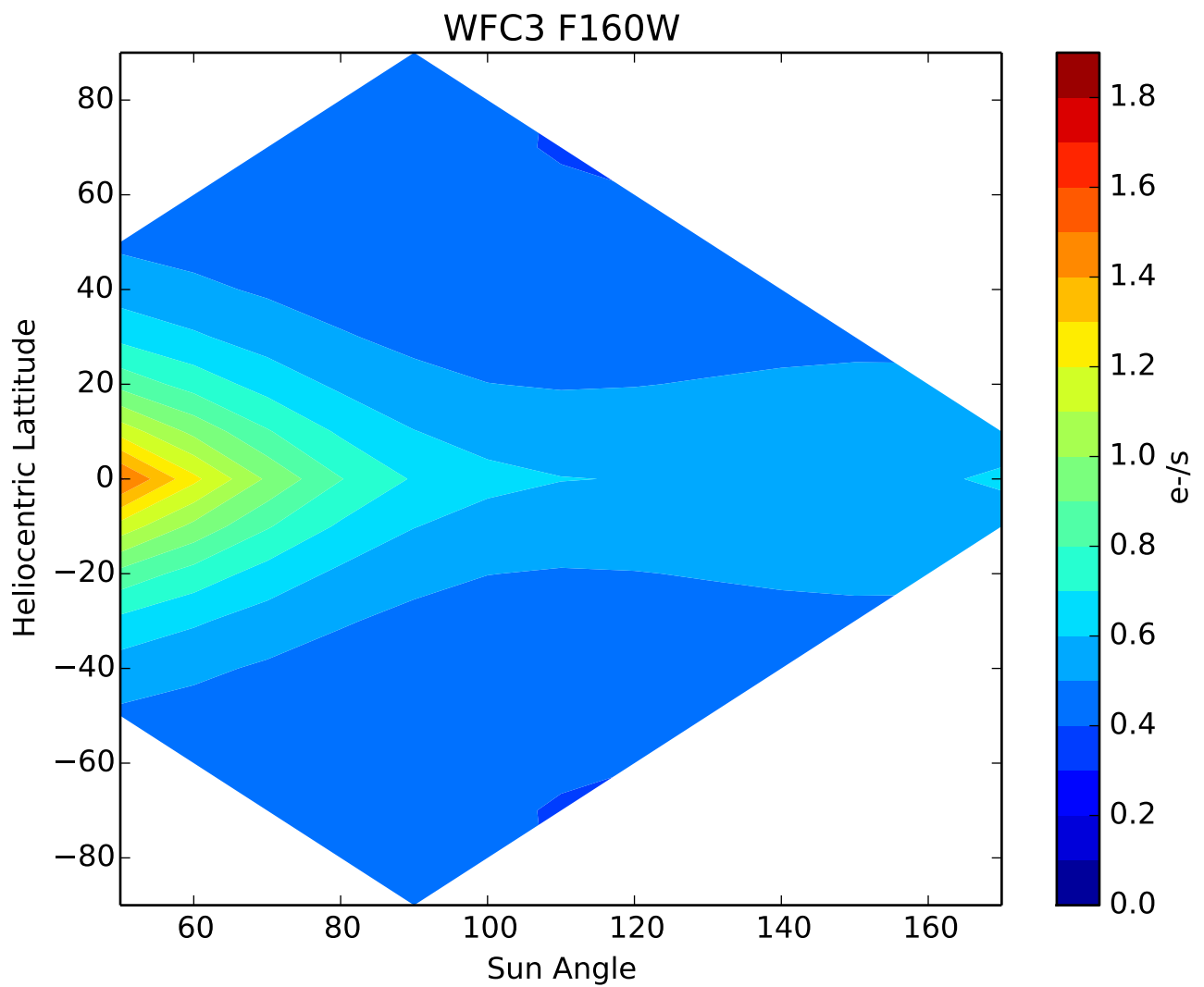


Fig. 4.— Our model of the F160W IR background in $e^-/s/pixel$ as a function of Sun Angle and Ecliptic Latitude.